FMCW BASED MIMO IMAGING RADAR FOR MARITIME NAVIGATION

Y. Huang and P. V. Brennan

Department of Electronic & Electrical Engineering
University College London
Torrington Place, London WC1E 7JE, United Kingdom

D. Patrick, I. Weller, P. Roberts, and K. Hughes

Guidance Microwave Ltd.
C2, Knowl Piece, Wilbury Way, Hitchin SG4 0TY, United Kingdom

Abstract—The berthing of large ships in inclement weather with frequently poor visibility presents a challenge. To assist with this application, it may be beneficial to utilise standard radar imaging. Whilst this may be achieved using a mechanically-scanned system, reliability, cost and weight issues, coupled with the need to primarily image only a 120° sector on the port and starboard of the ship, make phased array radar an attractive possibility. Multiple-Input Multiple-Output (MIMO) radar, with its ability to enhance the resolution available from a given number of elements, is particularly suited to a short-range application such as this in which there is sufficient time to switch between antenna elements as an alternative to more complex implementations. This paper describes a system of this nature from its basic architecture to development and validation, including some artefacts of the particular topology employed.

1. INTRODUCTION

Phased array radar employs a group of antennas to radiate and receive electromagnetic signals, the phases of which are adjusted so that the radar is able to scan or steer across the desired directions while suppressing the responses from other directions. This technique has been in place for many years and is now a reliable and popular option

for imaging radar. While the mechanism of phased array is well known, the recent combination of phase array with the MIMO concept [1] has led to an emerging area where lower cost and higher performance can be achieved simultaneously, making MIMO phased array radar an attractive candidate for short range imaging applications [2].

Basic phased array radar resolves directions of radar echo from passive targets by means of beam-forming techniques, whose angular resolution is limited by the relative size of the array to the signal wavelength [3]. In order to attain high angular resolution and adequate imaging quality, the phased array needs to be relatively large, but the spacing between elements is limited to half a wavelength to avoid grating lobes. Consequently, a large number of antenna elements in the array are required to build a larger array, which adds to the system complexity. Resolution beyond this limit can be achieved with advanced superresolution array processing methods [4–6], which increases the computation load and processing time. On the other hand, a MIMO arrangement of phased array antenna elements provides another possibility for achieving higher resolution with fewer elements.

This paper presents such a novel coherent MIMO phased array radar system that can be built with conventional off-the-shelf components. The detailed system design including architecture, antenna array, and signal model are given in the Section 2. By deramping the frequency modulated continuous wave (FMCW) signals, the proposed radar system is able to digitize received signals at a relatively low sampling rate and thus the imaging process is simplified. A prototype system of this design has been developed and the initial experimental imaging results are to be presented in Section 3.

2. MIMO PHASED ARRAY RADAR SYSTEM DESIGN

As implied by its name, MIMO radar consists of multiple antenna elements in both signal transmission and reception. For a coherent MIMO radar with M_t transmit (TX) elements and M_r receive (RX) elements, there are $M_t \times M_r$ distinct propagation channels from the TX array to the RX array. If the transmitting source (TX channel) of the received signals can be identified at the RX array, a virtual phased array of $M_t \times M_r$ elements [7] can be synthesized with only $M_t + M_r$ antenna elements. Diversity of the TX channels can be achieved by employing time division multiplexing, frequency division multiplexing, spatial coding, and orthogonal waveforms [8]. The virtually formed phased array can be designed to produce the desired pattern by arranging the placements of the TX and RX elements in an appropriate way [9–11].

2.1. Antenna Array Architecture

The coherent MIMO phased array radar proposed in this paper consists of a sparsely separated RX array in the middle and two groups of TX elements surrounding the RX array. Fig. 1 shows an example array with 4 TX and 16 RX antenna elements, synthesizing a uniform linear array (ULA) of 64 virtual elements. Placement of the physical TX and RX antenna elements, as well as the resultant virtual array, is illustrated by Fig. 1.
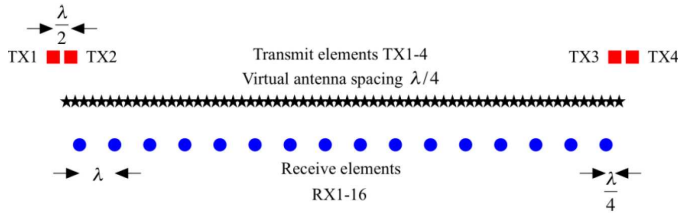

Figure 1. Illustration of the 20-element MIMO radar topology developed in this work.

This is a symmetrical linear arrangement of the TX and RX elements, with some vertical offset between the TX array and the RX array for reduced coupling. Note the coordinates of the TX elements as x_i^{Tx}, $i = 1, 2, 3, 4$, and the coordinates of the RX elements as x_j^{Rx}, $j = 1, 2, \ldots, 16$. By arranging the TX elements and RX elements in the way shown by Fig. 1, a total of $M_t \times M_r = 64$ distinct virtual elements can be formed. If the far field condition is met [10], the signal propagation from a TX elements x_i^{Tx} to a point scatterer $\mathbf{p}$ plus reflection path from $\mathbf{p}$ to RX elements can be approximated by the return path between the corresponding virtual element $x_{ij} = (x_i^{Tx} + x_j^{Rx})/2$, and the scatterer $\mathbf{p}$:

$$P_{ij}(p) = \left| \mathbf{p} - x_i^{Tx} \right| + \left| \mathbf{p} - x_j^{Rx} \right| \approx 2 \left| \mathbf{p} - x_{ij} \right| \tag{1}$$

The resultant 64 virtual elements synthesized from the 20 elements shown in Fig. 1 are distributed along the middle line (stars in black) between the TX and the RX array.

The rule for designing such a coherent MIMO array with non-overlapping equally spaced elements is simple. If the desired virtual element spacing d is given, the interelement spacing in either group of the TX array needs to be $d_t = 2d$, the interelement spacing in the RX array shall be $d_r = M_t d$, and the gap between each $M_t/2$-element TX group and the edge element of the RX array, d_{tr}, is equal to d. By fulfilling these requirements, a virtual ULA of $M_t \times M_r$ elements

separated by d can be formed in signal processing. The physical length of this MIMO array is $(M_t M_r + M_t - 2)d$, and the length of the virtual array is $(M_t M_r - 1)d$.

As for the example in the Fig. 1, elements in the RX array are separated by λ. The TX array is divided into two groups of two elements, placed at both sides of the RX array. The interelement spacing of the TX array is 0.5λ which ensures that the resultant virtual elements are spaced by 0.25λ to avoid grating lobe. The virtual element spacing would seem to be one half of the conventional 0.5λ spacing requirement of the classic phased array. A receive-only or transmit-only phased array experiences a one-way path delay to any location and would indeed require 0.5λ spaced elements to avoid grating lobes. However the MIMO array presented here both transmits and receives from each virtual element position and so a two-way path delay is experienced to a given target. Thus the virtual element positions need to be spaced by 0.25λ in order to avoid grating lobes.

2.2. FMCW Signal Model

The TX array elements transmit a frequency-modulated continuous wave (FMCW) chirp signal, which can be modelled as:

$$s(t) = \exp[j(2\pi f_c t + \pi k t^2)]; \quad -T_c/2 \leq t \leq T_c/2 \tag{2}$$

where T_c is the chirp duration, f_c is the carrier frequency, and k is the chirp rate defined by the chirp sweeping bandwidth divided by the chirp duration.

$$k = \pm B/T_c \tag{3}$$

Positive chirp rate k represents up-chirp and negative k stands for down-chirp.

Assuming that the far field condition is fulfilled, the return delay between a virtual element at x_{ij} and a scatterer at rang R and angle θ (with respect to boresight) can be expressed as

$$\Delta t_{ij} = \frac{2R}{c} + \frac{2x_{ij}\sin\theta}{c} \tag{4}$$

Therefore, the received signal $r_{ij}(t)$ at element x_{ij} a delayed and attenuated version of the transmitted chirp defined in the Eq. (2)

$$r_{ij}(t) = A \cdot s(t - \Delta t_{ij}) \tag{5}$$

where A represents the combined effect of propagation loss and antenna gains, assuming time-invariance and equal amplitude at each element in this case.

The received chirp signals at the RX array are then processed using a deramp technique, which involves multiplying the received

signal with the transmitted chirp replica, followed by low-pass filtering [12], which process can be modelled as

$$u_{ij}(t) = r_{ij}^*(t)s(t) = [A \cdot s^*(t - \Delta t_{ij})] \cdot s(t)$$
$$= A \cdot \exp\left[j\left(2\pi k \Delta t_{ij}t - \pi k \Delta t_{ij}^2 + 2\pi f_c \Delta t_{ij}\right)\right] \quad (6)$$

As can be seen, both the range and bearing information are included in the result from the deramp processing given in the Eq. (6).

Firstly, deramping the received signals effectively converts time delay into the frequency domain, as indicated by the frequency term of the deramp result, $2\pi k \Delta t_{ij}t$. Frequencies of the deramped signals from the jth RX element for the ith TX transmit channel are defined by

$$f_{ij} = k\Delta t_{ij} \approx 2kR/c \quad (7)$$

Apparently Δt_{ij} is dominated by $2R/c$ under far field conditions, and thus is a constant value along all the virtual channels. More importantly, this frequency value is directly proportional to the range R, allowing the system to retrieve the range information from a simple FFT analysis. Every frequency sample in the frequency domain represents a specific range bin that is linearly proportional to its frequency by $c/2k$. Therefore, the range resolution is limited by the frequency resolution, which is inverse to the chirp duration T_c. It can be found that the range resolution is defined by the bandwidth of the transmitted chirp:

$$\Delta R = \frac{c}{2k}\frac{1}{T_c} = \frac{c}{2B} \quad (8)$$

Secondly, the phase term in Eq. (6) reflects the arrival angle of the echo, which can be found by beamforming with the adequate steering vectors.

The phase term in Eq. (6) contains a linear component $2\pi f_c \Delta t_{ij}$, and a squared component $\pi k \Delta t_{ij}^2$ of the delays. It shall be noted that, for a scatterer within the detectable range of the radar, the squared component is nearly constant for all the virtual channels. The deramped phase term can therefore be expressed as the sum of a phase component dependent on the element coordinates and a constant dependent on the scatterer range.

$$\varphi = 2\pi f_c \Delta t_{ij} - \pi k \Delta t_{ij}^2 = 2\pi f_c \frac{2x_{ij}\sin\theta}{c} + 2\pi f_c \frac{2R}{c} - \pi k \Delta t_{ij}^2$$
$$= 4\pi \frac{x_{ij}\sin\theta}{\lambda} + C \quad (9)$$

The $4\pi/\lambda$ factor in the Eq. (9) reflects the two-way path delay as modelled by the Eq. (4). As compared to the $2\pi/\lambda$ factor for the

conventional transmit-only or receive-only phased array, the phase term given in the Eq. (9) therefore validates the 0.25λ grating-lobe-free spacing requirement.

There are $M_t M_r$ deramped results in the form of Eq. (6). The steering vectors that can be used to resolve the relative angle of the scatterer are given by the Kronecker product of the steering vector for the TX array and the steering vector of the RX array. The transmitting steering vector is written as

$$a_i^{Tx}(\theta) = \exp\left(-j2\pi\frac{x_i^{Tx}\sin\theta}{\lambda}\right); \quad i = 1, 2, \ldots, M_t \tag{10}$$

While the receiving steering vector is

$$a_j^{Rx}(\theta) = \exp\left(-j2\pi\frac{x_j^{Rx}\sin\theta}{\lambda}\right); \quad j = 1, 2, \ldots, M_r \tag{11}$$

Given that $x_{ij} = (x_i^{Tx} + x_j^{Rx})/2$, the steering vector for the virtual array is thus

$$a_{ij}(\theta) = a_i^{Tx}(\theta) \otimes a_j^{Rx}(\theta) = \exp\left[-j2\pi\frac{\left(x_i^{Tx}+x_j^{Rx}\right)\sin\theta}{\lambda}\right]$$

$$= \exp\left[-j4\pi\frac{x_{ij}\sin\theta}{\lambda}\right] \tag{12}$$

where $i = 1, 2, \ldots, M_t$, and $j = 1, 2, \ldots, M_r$. As can be seen, it is in the negative form of the first phase component given by Eq. (9). Subsequently, beamforming of the MIMO array signals can be regarded as synthesizing the received signals with the two-way steering vector, Eq. (12), generated from the coordinates of the virtual elements.

For a given range $R = cf/2k$, computed by Eq. (7), the azimuth profile can be found by

$$P(\theta) = \sum_{i=1}^{M_t}\sum_{j=1}^{M_r}\mathbf{U}(f) \cdot a_{ij}(\theta) \tag{13}$$

where $\mathbf{U}(f)$ is the spectrum of the deramp signals given by Eq. (6).

The angular resolution $\Delta\theta$ at a given angle θ from beamforming is dependent on the effective aperture A_e of the virtual array:

$$\Delta\theta = \frac{\lambda}{2A_e} = \frac{\lambda}{2\left(M_t M_r - 1\right)d \cdot \cos(\theta)} \tag{14}$$

The cross range resolution for a position (R, θ) can be approximated by the product of angular resolution and the range:

$$\delta R \approx \Delta\theta \cdot R = \frac{\lambda R}{2\left(M_t M_r - 1\right)d \cdot \cos(\theta)} \tag{15}$$

The model for using the FMCW signal with the proposed coherent MIMO array for image processing has been summarized in this section. It has shown that a 2-D image can be obtained from the received channels of samples, by performing Eq. (13) for the full detection range. The range resolution and the angular resolution are given by Eq. (8), and Eq. (14) respectively.

2.3. Transmit Diversity by Switching

In order to synthesize the total number of $M_t M_r$ MIMO channels, the signal processing shall be able to differentiate the TX channels and separate the time samples according to their originating TX sources. A simple yet reliable method is time division, switching the TX channels on or off for radiation at different time slots.

Consider the 4 TX and 16 RX array given in the Fig. 1, with the switching TX scheme, the TX elements are activated in turn by a four-way RF switch while the RX elements are receiving microwave signals in parallel and synchronously.

The transmission scheme for this case is given in a time-frequency diagram in Fig. 2, which shows the frequency sweeping characteristics of both transmitted and reflected chirps over time in the time slots for the four TX channels.
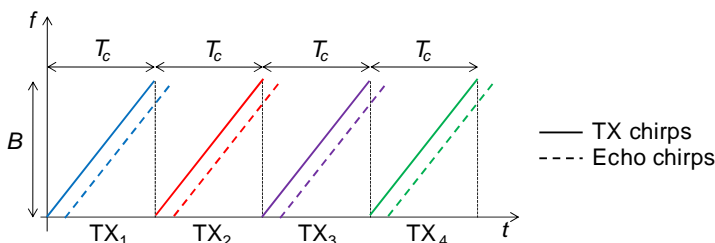

Figure 2. Transmission scheme for 4-TX elements array.

Reception of signals for the four slots makes a cycle of "scan". The total $M_t M_r$ channels of signals are found and an image can be produced when the reflected signals from all the TX slots are received. If the chirp duration is designed to be much longer than the two-way propagation delay corresponding to the furthest detection range ($\tau = 2R_{\max}/c \ll T_c$), the range and angle information carried by the received signals can be retrieved at the resolutions defined by Eqs. (8) and (14).

Longer chirp duration is usually desirable as it not only ensures the designed resolution but also delivers greater energy to the scatterer,

and thus increases the received echo power. However, the chirp duration of FMCW radar is also limited by other practical conditions.

Firstly, the conventional limit on chirp duration due to the target acceleration also applies to this coherent MIMO design. It is defined that the change of radian frequency Δf_d over one chirp duration, T_c, should not be greater than the frequency resolution $1/T_c$, as otherwise the measurement of the scatterer will be blurred and a false phantom target will appear besides the real target. This condition suggests an upper bound for the chirp duration, noted as T_s.

The Doppler frequency resulting from target movement at the speed of v can be modelled as:

$$f_d = \frac{2}{\lambda} v \tag{16}$$

If the target is accelerating, this frequency term will vary too. According to the condition discussed above, the change of Doppler frequency within one chirp duration shall be smaller than the frequency resolution:

$$\Delta f_d = \frac{2}{\lambda} \frac{dv}{dt} T_c = \frac{2a}{\lambda} T_c \leq \frac{1}{T_c} \tag{17}$$

where a is the acceleration rate of the target. Eq. (16) therefore sets the upper bound on the chirp duration by

$$T_s < \sqrt{\frac{\lambda}{2a_{\max}}} \tag{18}$$

where $a_{\max}$ is the maximum possible acceleration of a target that the system is trying to detect.

However, it is not the most significant restriction in case of switching transmission MIMO radar, as the upper bound set by the target acceleration is looser than that given by the target velocity.

In terms of the switching transmission scheme, since imaging of the environment requires full reception of all M_t slots of signals, it practically induces a physical relationship between the velocity of a target and the chirp duration. That is, from the first TX slot until the last TX slot, the movement of a target shall not exceed a nominal quarter wavelength, to maintain coherent beamforming. The acceptable average target velocity v is therefore defined by

$$(M_t - 1) \cdot T_c \cdot v < \lambda/4 \tag{19}$$

which sets an upper bound for the chirp duration as

$$T_M < \frac{\lambda}{4(M_t - 1) \cdot v} \tag{20}$$

To compare these two bounds, let us consider a maritime example where a ship target is moving at the speed of $v = 20\,\text{m/s}$, with acceleration of $a = 10\,\text{m/s}^2$. To image it properly, the maximum chirp durations restricted by Eq. (18) and Eq. (20) are 40 ms and 0.135 ms respectively. It is obvious that the condition derived from Eq. (20) is much stricter. Therefore, compared to conventional single pulse radar, the proposed coherent MIMO radar using switching transmission scheme is constrained by the Eq. (20) to use shorter chirp duration, which results in less power being transmitted and thus reduced radar detection range.

On the other hand, since the energy carried by a radar signal is proportional to its duration, and the two-way path loss for point targets is proportional to range to the power of four, the reduction in radar detection range caused by shorten chirp duration can be estimated by

$$\frac{R_M}{R_s} \propto \left(\frac{Mt * T_M}{T_s} \right)^{1/4} \tag{21}$$

where T_M and R_M are maximum chirp duration and maximum detection range for the switched-TX MIMO radar design, while T_s and R_s are corresponding maximum figures for single pulse radar.

Consider the example discussed above, where $T_M = 0.135\,\text{ms}$ while $T_s = 40\,\text{ms}$, the maximum detection range for the switching-TX MIMO radar is about a third of that for the single pulse radar.

$$R_M = 0.34 \cdot R_s \tag{22}$$

That is to say, the simplicity and high-quality inter-channel isolation provided by the switching-TX scheme are obtained by sacrificing the tolerable target velocity and maximum radar detection range. If this trade-off is not affordable, orthogonal transmission schemes can be consider, where new issues such as isolation between TX channels and raised noise floor may occur.

2.4. System Architecture

A demonstration system for the proposed coherent MIMO radar has been developed. The system specifications are listed in the Table 1. It consists of a direct digital synthesizer (DDS) based chirp generator, the MIMO antenna array, chirp deramping unit, IF signal processor, analog-to-digital converter (ADC), and the signal processing modules implemented in LabView. The block diagram given in the Fig. 3 shows this compact yet self-contained design.

The antenna array used in this system has been presented in the Fig. 1, which transmits FMCW chirp signals sweeping over 100 MHz at the 9.25 GHz band. The mean wavelength is therefore $\lambda = 3.24\,\text{cm}$.

Table 1. System specifications.

Centre frequency	9.25 GHz	Detection range	253 m
Chirp bandwidth	100 MHz	Angle range	120°
Single chirp duration	135 μs	Sampling rate	2.5 MSps
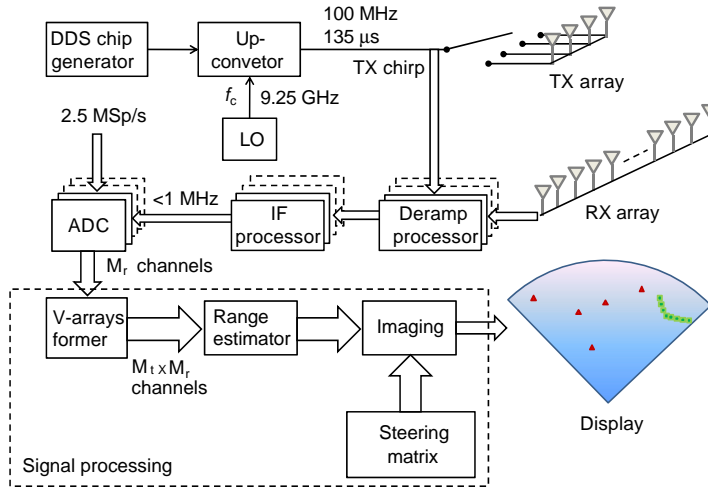
Figure 3. Block diagram of the MIMO phased array radar system.

According to the 0.25λ virtual element spacing setting mentioned above, the length of the MIMO array is therefore 53.5 cm while the virtual array aperture is 51.1 cm. In practice, the TX array and the RX array are offset by 3λ vertically, in order to reduce coupling from TX to the RX channel, as can be seen from Fig. 1.

The TX chirp is chosen to be 135 μs long in time. The chirp modulation rate k is 740.7 kHz/μs in this case. The baseband version of this chirp is generated with a DDS module and it is up-converted to X-band using a PLL-based design to produce the TX chirp.

The chirp signal is then fed to a four-way RF switch whose outputs are linked with the 4 TX elements. The switch is programmed to connect one TX element each time as explained in Section 2.3. Therefore, a full "scan" lasts for 4×135 μs $= 540$ μs in time.

Each TX or RX element uses a 6 dBi gain rectangular patch antenna with two vertically arranged radiators. The elevation beamwidth of this element is 60° while the azimuth beamwidth is 120°.

Echo signals are received by the 16 RX elements simultaneously and deramp processing is applied directly beyond reception of the signals by means of an RF mixer, which mixes the transmitted chirp with the received echoes and producing IF signals whose frequencies are proportional to range of targets (as shown by Eq. (7)).

The IF signals are firstly high-pass filtered to compensate the range dependant propagation loss before being sampled by two synchronized 8-channel data acquisition cards (DAQ), at the rate of 2.5 MSps. The converted digital signals are read into a PC and further processed in a LabView program. According to Nyquist theorem, the highest resolvable frequency in signal processing is half the sampling rate, which is 1.25 MHz, corresponding to approximately 253 m, which is the maximum radar detection range (refer to Eq. (7)).

In the digital signal processing, the total 16 channels of data are firstly reorganized into 64 channels of echoes, each of which contains 338 samples. Fast Fourier transform (FFT) is applied along all the 64 channels of data so that the range information can be resolved using Eq. (7). The steering matrix defined by Eq. (12) is pre-calculated and used to resolve the bearing information from the FFT results. Supperresolution techniques (e.g., MUSIC) can also be used in either range or azimuth profile in order to achieve even better image quality at the cost of longer processing time.

With the beamforming method, the range resolution is 1.5 m, as given by the Eq. (8). The length of the array is 0.51 m, and thus the angular resolution at the boresight is approximately 1.8°, according to the Eq. (14). Therefore, the cross range resolution, given in Eq. (15), on the other hand is a function of the distance. A few examples of cross range resolution have been listed in the Table 2.

Table 2. Cross range resolution at various ranges.

Distance	20 m	50 m	100 m	200 m
Cross range resolution	0.64 m	1.59 m	3.18 m	6.36 m

3. FIELD TRIAL RESULTS WITH THE PROTOTYPE SYSTEM

To examine the performance of the proposed coherent MIMO array radar, the demonstration system has been tested in a field trial and the results show good agreement between the theoretical analyses and the measured images. The site chosen for the field trial is a football court which is surrounded by trees and a road, as can be seen from the Fig. 6.

3.1. Image Resolution

A test on the image resolution has been executed in the trial site, using two corner reflectors as point targets. The corner reflectors are placed at roughly 20 m away from the MIMO array and are separated at various distances in both range and cross range directions. Ordinary beamforming and FFT processing, as given in the Section 2, of the 64 channels deramped signals are used to image the corner reflectors.

In the first experiment, the two point targets are offset by 1.5 m away from each other in the range direction, while separated by 1 m in cross range direction (equivalent to 3o angular separation), as can be seen from the upper diagram of the Fig. 4. A small portion of the imaging result, showing ±45o angles and 18 m to 28 m range, is given in the Fig. 4.
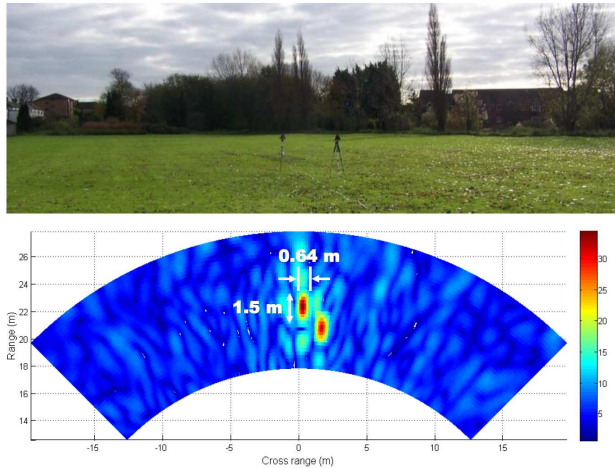

Figure 4. Two corner reflectors separated by 1.5 m in range and 1 m (apx. 3°) in cross range.

The two corner reflectors appear as two oval shape red dots in the image (Fig. 4). This is because the range resolution (1.5 m) is about 2.3 times the cross range resolution (0.64 m), at 20 m range. Both the separation in range and cross range directions are seen clearly in this diagram. One of the corner reflectors appears at roughly (20.8 m, 2o), while the other one appears at (22.3 m, 5o), reflecting the actual placement of the two corner reflectors.

In another resolution test, the two corner reflectors are placed very close to each other, with roughly 0.64 m separation in cross range and zero offset in range, Fig. 5. The two dots seen from the imaging
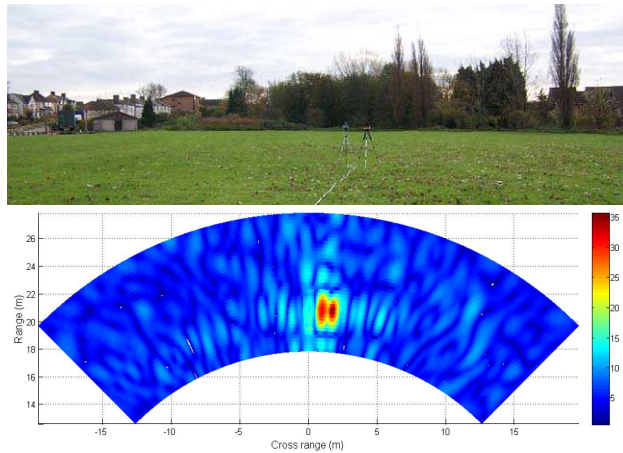
Figure 5. Two corner reflectors separated by 0 m in range and 0.64 m (apx. 1.8°) in cross range.

result are barely differentiated from each other in the diagram. This is because their separation just reached the theoretical resolution as given in Table 2.

The imaging results shown in this section have validated the MIMO array processing technique using FMCW signals. Both the range and cross range resolution, estimated from the theoretical analysis, are demonstrated by experiments.

3.2. Imaging Surrounding Environment

As introduced, the MIMO array radar system was set up at one end of the field and was used to image an area specified by the yellow fan shape area indicated by Fig. 6, which is a satellite image of the trial site.

Imaging result of the environment is given in Fig. 7, which is obtained from MUSIC processing for azimuth profile and FFT processing for resolving the range information. The empty field is displayed as a large blue area in the middle of the radar image. Locations and shapes of the nearest layer of the surrounding trees are clearly seen. Even the gaps among the trees can be identified as well, as indicated by two arrows in the satellite photo.

At about 200 m away, a few buildings in that area, marked by the larger red circle A in Fig. 6, are also seen. Another smaller building at the location of circle B is displayed as a rotated rectangular shaped dot as well.
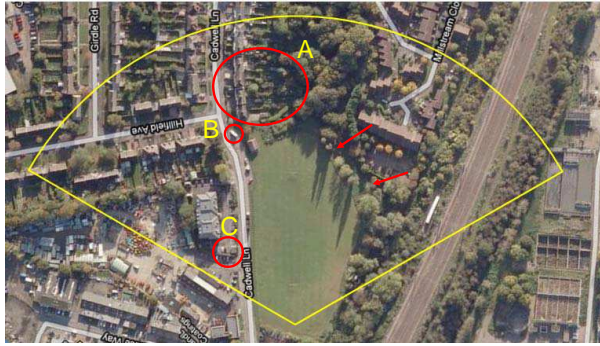
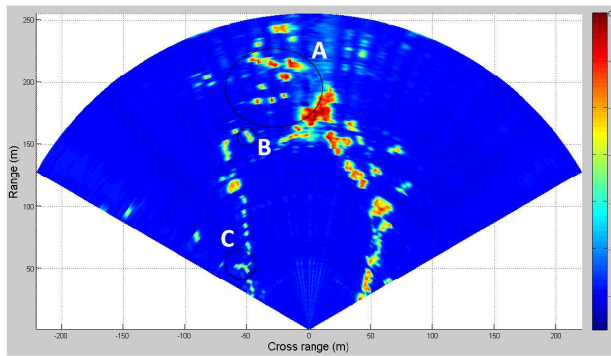**Figure 6.** Satellite image of the trial site (source: Google maps).

Figure 7. Example image from the MIMO radar system (using MUSIC algorithm).

On the left hand side, there are a row of smaller trees that are planted along the road and they appear at the corresponding locations in the radar image as a row of dots too. At the location marked by circle C, there is a building that is present as a laid-down "Y" in the radar image.

It shall be noted that, most of the area beyond the nearest layer of obstacles are in the radar shadow and therefore not many echoes are reflected from these areas. However, there are a few yellow dots of various sizes seen beyond the nearest layer of obstacles, which is because some transmitted signals were leaked through the gaps of the trees to further areas.

The radar images shown above have demonstrated the imaging performance of the proposed coherent MIMO array radar. Responses for corner reflectors have the resolutions expected from theoretical

analysis. Imaging of the environment allows us to see a number of obstacles present in the satellite image.

4. CONCLUSION

In this paper, a novel coherent MIMO array radar based on FMCW signals is described, from the physical MIMO array design to the signal model. The imaging processing theory has been derived and analyzed too to estimate the image quality. Some useful practices for designing the MIMO array and the waveform have been summarized as well and fulfilment of these guidelines ensure proper operation of the imaging radar.

A demonstration radar system based on a 4 TX and 16 RX array, operating at 9.25 GHz band, is therefore implemented using the theories derived. The same methodology can be used to design other linear arrays, at different frequencies, depending on the image resolution requirements and the available sampling rate.

As can be seen, the demonstrated image quality agrees very well with the theoretical expectation presented in the Section 2 of this paper. Closely placed point targets can be differentiated in the image at the resolutions defined. When this radar is used to image the surrounding environments, clear and accurate representations of the obstacles in the area monitored are seen from the radar image.

The compact and cost efficient MIMO array design is desirable in many new and promising applications [13]. The compact structure of the antenna array does not require mechanical control and thus can be installed in places where it would be impossible for mechanical radar. For example, in the maritime application, image of quays or docks may aid berthing of large ship and thus improve the efficiency of port.

REFERENCES

1. Fishler, E., A. Haimovich, R. Blum, D. Chizhik, L. Cimini, and R. Valenzuela, "MIMO radar: An idea whose time has come," *Proceedings of the IEEE Radar Conference, 2004,* 71–78, 2004.
2. Soldovieri, F. and N. Romano, "The mutual interaction between the reconfigurable transmitting and receiving antennas in ground penetrating radar surveys," *Journal of Electromagnetic Waves and Applications*, Vol. 23, No. 14–15, 1919–1928, 2009.
3. Wirth, W.-D., *Radar Techniques Using Array Antennas,* The Institution of Electrical Engineers, 2001.

4. Schmidt, R., "Multiple emitter location and signal parameter estimation," *IEEE Transactions on Antennas and Propagation*, Vol. 34, No. 3, 276–280, Mar. 1986.

5. Roy, R., A. Paulraj, and T. Kailath, "Estimation of signal parameters via rotational invariance techniques — ESPRIT," *IEEE Military Communications Conference — Communications-computers: Teamed for the 90's*, 3rd edition, 41, 1986.

6. Yang, P., F. Yang, and Z.-P. Nie, "DOA easimation with sub-array divided technique and interpolated ESPRIT algorithm on a cylindrical conformal array antenna," *Progress In Electromagnetics Research*, Vol. 103, 201–216, 2010.

7. Jian, L., P. Stoica, and Z. Xiayu, "Signal synthesis and receiver design for MIMO radar imaging," *IEEE Transactions on Signal Processing*, Vol. 56, No. 8, 3959–3968, Aug. 2008.

8. Wang, G. and Y.-L. Lu, "Sparse frequency waveform design for MIMO radar," *Progress In Electromagnetics Research B*, Vol. 20, 19–32, 2010.

9. Qu, Y., G. Liao, S.-Q. Zhu, X.-Y. Liu, and H. Jiang, "Performance analysis of beamforming for MIMO radar," *Progress In Electromagnetics Research*, Vol. 84, 123–134, 2008.

10. Ender, J. H. G. and J. Klare, "System architectures and algorithms for radar imaging by MIMO-SAR," *IEEE Radar Conference 2009*, 1–6, 2009.

11. Zhang, X., X. Gao, G. Feng, and D. Xu, "Blind joint DOA and DOD estimation and identifiability results for MIMO radar with different transmit/receive array manifolds," *Progress In Electromagnetics Research B*, Vol. 18, 101–119, 2009.

12. Lacomme, P., J.-P. Hardange, J.-C. Marchais, and E. Normant, *Air and Spaceborne Radar Systems — An Introduction*, William Andrew Publishing/Noyes, 2001.

13. Le Marshall, M. W. D. and A. Z. Tirkel, "MIMO radar array for termite detection and imaging," *Progress In Electromagnetics Research B*, Vol. 28, 75–94, 2011.